Applied Surface Science 513 (2020) 145787

Contents lists available at ScienceDirect

Applied Surface Science

journal homepage: www.elsevier.com/locate/apsusc

Full Length Article

Stabilization of the perovskite phase in PMN-PT epitaxial thin films via increased interface roughness

Urška Gabor[a,b,c,*], Damjan Vengust[a], Zoran Samardžija[d], Aleksander Matavž[b,e], Vid Bobnar[b,e], Danilo Suvorov[a], Matjaž Spreitzer[a]

[a] Advanced Materials Department, Jožef Stefan Institute, Jamova cesta 39, 1000 Ljubljana, Slovenia
[b] Jožef Stefan International Postgraduate School, Jamova cesta 39, 1000 Ljubljana, Slovenia
[c] Peter Grünberg Institut 7, Forschungszentrum Jülich GmbH, 52428 Jülich, Germany
[d] Department for Nanostructured Materials, Jožef Stefan Institute, Jamova cesta 39, 1000 Ljubljana, Slovenia
[e] Condensed Matter Physics Department, Jožef Stefan Institute, Jamova cesta 39, 1000 Ljubljana, Slovenia

ARTICLE INFO

Keywords:
PLD
PMN-PT thin film
Pyrochlore
Bottom electrode
Sticking coefficient

ABSTRACT

Pulsed-laser deposition was used to prepare $Pb(Mg_{1/3}Nb_{2/3})O_3$-$PbTiO_3$ (PMN-PT) thin films on ($LaNiO_3$)/$SrTiO_3$ substrates. We found that the bottom electrode has an immense influence on the properties of the overgrown active layer. Specifically, we found that the use of $LaNiO_3$ (LNO) as the electrode material strongly stabilizes the perovskite phase and significantly expands the process window for the preparation of phase-pure PMN-PT as compared to a direct deposition on $SrTiO_3$ (STO) substrates. Based on our experiments, the stabilization is achieved primarily due to the increased interface roughness, which enhances the sticking of Pb-based species, thereby suppressing the formation of undesired Pb-deficient pyrochlore inclusions. The roughness of the interface does not have adverse effects on the quality of the films. In fact, the film prepared on the LNO/STO template from the Pb-rich target exhibited superior electrical properties as compared to the film prepared directly on STO. By understanding the mechanism, we were able to exploit it and prepare an STO/Nb:STO template with a rough surface, which strongly enhanced the stability of the perovskite phase. This approach can be used to design templates for different device configurations.

1. Introduction

Exceptional electromechanical coupling and high relative permittivities with weak temperature dependences make Pb-based relaxor-ferroelectrics attractive for a plethora of applications. A large amount of research has been focused on finding the origin of giant piezoelectricity in these solid solutions with compositions around the morphotropic phase boundary [1–6]. Understanding the origin of the enhanced properties as well as identifying the growth mechanisms can offer valuable guidance for designing new piezoelectrics, including lead-free alternatives. The ultrahigh piezoelectricity can be utilized in devices such as sensors, actuators or energy harvesters, as it has been shown with epitaxial thin films of $Pb(Mg_{1/3}Nb_{2/3})O_3$–$PbTiO_3$ (PMN-PT) [7]. Additionally, PMN-PT thin films exhibit excellent properties for pyroelectric/electrocaloric energy scavenging and cooling [8–10] and energy storage [11]. In order to exploit the material's full potential, however, it is imperative to prepare it in phase-pure form.

As with other Pb-based materials that are processed at elevated temperatures, one of the key issues related to the preparation of crystalline PMN-PT is the loss of Pb, owing to its high vapor pressure. This issue is well known in the literature. Different regulation mechanisms have been proposed, the main goal mostly being the elimination of the undesired Pb-deficient pyrochlore phases, which degrade the piezoelectric properties. The most common approach in thin-film synthesis by means of pulsed-laser deposition (PLD) involves adjusting the process parameters in such a way that the evaporation of Pb from the heated substrate surface is minimized. This includes lowering the deposition temperature, increasing the deposition rate by increasing the energy density and/or pulse frequency of the laser, etc. [12–18]. The second approach involves using substrates with a higher miscut, where the higher step density provides more binding sites for Pb, thereby retaining it in the thin-film structure [7,19,20]. The third approach is based on the compensation of the evaporated Pb by employing Pb-enriched targets [12,14,21]. There are also additional less commonly used approaches, such as dual-laser ablation [22], for example. All of the abovementioned approaches can be (and often are) used in conjunction.

* Corresponding author at: Advanced Materials Department, Jožef Stefan Institute, Jamova cesta 39, 1000 Ljubljana, Slovenia.
E-mail address: urska.gabor@ijs.si (U. Gabor).

https://doi.org/10.1016/j.apsusc.2020.145787
Received 1 September 2019; Received in revised form 7 January 2020; Accepted 14 February 2020
Available online 15 February 2020

The optimization process is usually based on analyzing the phase composition of the films by X-ray diffraction (XRD). Rarely, other techniques are employed to determine the stoichiometry of the ablated target [23], transfer of material in the plume [17,23] and the final chemical composition of the films [7,12].

For the purpose of electrical characterization, the films are almost always grown on substrates that are already covered with a bottom electrode. Capacitors with metallic electrodes, such as Pt, exhibit poor retention and relatively high fatigue. Oxide electrodes can drastically improve fatigue behavior [24,25]. Different mechanism have been proposed to explain this improvement, such as oxide electrodes acting as an oxygen vacancy sink [26] or enhanced relaxation of the charge injected by the electrodes [27,28]. Furthermore, it is well known that the phase purity and epitaxial arrangement of Pb-based films improves when the films are grown on oxide electrodes [15,24,29,30]. Contrarily, the influence of the individual oxide electrodes has not been studied in much detail. While there are some reports on the influence of different oxide electrodes, they are mostly focused on the domain structures [31–33], strain [34,35] and ferroelectric properties [36]. The influence of the bottom electrode on the growth mode has been studied in $BiFeO_3$ (BFO) thin films. BFO films grown directly on $SrTiO_3$ (STO) substrates reportedly exhibited island growth, whereas the ones grown on an $SrRuO_3$ (SRO) electrode layer remained atomically flat [31]. Although these studies have considered many different aspects, an important one has been overlooked, namely the influence of the bottom electrode on the phase composition of the films. As described, this is an especially important aspect in the growth of Pb-based films, such as PMN-PT, where the thermodynamic stability of the perovskite phase is often low at the temperatures required for obtaining films with a high crystalline quality. Changing the interface type can affect the sticking probability of the Pb-based species and thereby the phase composition of the films.

In this study we used PLD to grow PMN-PT thin films on different templates. PLD enables the growth of a large selection of materials in a broad range of experimental conditions. It is a versatile tool, which at the same time offers atomic-scale precision. Furthermore, in the past years, large-area deposition tools have been made commercially available. These tools enable wafer-scale high-quality thin-film growth [37–39]. Combined with relatively low-cost materials such as $LaNiO_3$ (LNO) and STO, which can be integrated with large Si wafers through existing processes [39], this study is focused on industrially-relevant materials and techniques. We compared the growth of PMN-PT thin films directly on STO substrates and on STO substrates with a LNO bottom electrode. The former can be used in piezoelectric energy harvesting (EH) devices operating in the longitudinal (d_{33}) mode, while the latter are appropriate for the transverse (d_{31}) mode. Theoretically, the power output of the EH is enhanced by implementing the d_{33} mode [40]. However, the growth of PMN-PT directly on STO is very challenging [14], requiring a high amount of PbO excess to eliminate secondary phases. This differs from literature reports where single-phase PMN-PT has been grown from stoichiometric targets on STO substrates covered by different bottom electrodes [13,41,42]. Therefore, we grew PMN-PT on both STO and LNO/STO templates under similar conditions using the same PLD system, which enabled a direct comparison of the two heterostructures. The observed strong stabilization of the perovskite phase on LNO/STO sparked further interest in the influence of the bottom electrode on the growth. In order to unravel the mechanism behind the enhanced stabilization, we deposited PMN-PT on other templates and analyzed the differences between the templates in detail. Furthermore, we analyzed the chemical composition and electrical characteristics of the films with the stabilized perovskite phase.

2. Materials and methods

2.1. Target and sample preparation

The STO (Plasmaterials) target was single-crystalline. The PMN-33PT (SolMateS) and $SrRuO_3$ (SRO) (Beijing Goodwill Metal Technology) targets were polycrystalline. The purity of all targets was > 99.9%. The PMN-33PT target with 20 mol. % PbO excess was prepared in-house. The detailed preparation procedure is described elsewhere [14]. A buffered hydrofluoric acid etch followed by annealing in oxygen at 950 °C was used to ensure TiO_2 termination of (0 0 1)-oriented STO substrates [43]. Some of the low miscut (< 0.5°) substrates were doped with 0.5 wt% Nb (CysTec), whereas all of the high miscut (4°) substrates undoped (SurfaceNet). The PMN-PT thin films were grown using a PLD system from Twente Solid State Technology. A KrF excimer laser (Coherent COMPex 205) with a 20 ns pulse and a wavelength of 248 nm was used for the ablation. Resistive heating was employed to reach the deposition temperature of 570 °C, which was measured by a *K*-type thermocouple. The base pressure for all depositions was kept under 1×10^{-7} mbar, while the oxygen pressure during the depositions was 0.27 mbar. A spot size of 2.3 mm^2, laser energy density of 2.25 J cm^{-2}, laser-pulse frequency of 8 Hz and target-to-substrate distance of 55 mm were selected for all of the experiments, and the samples were cooled to room temperature immediately after the depositions at a rate of 10 °C min^{-1} in 700 mbar O_2. In samples with LNO bottom electrodes the electrode layer was deposited first using the same parameters as for PMN-33PT except for the process pressure, frequency and laser energy density, which were 0.13 mbar, 5 Hz and 2.5 J cm^{-2}, respectively. The thickness of the standard LNO electrode layers was 100 nm, while the ultra-thin LNO layer was approximately 1.5 nm thick. The thickness of the PMN-33PT films was approximately 700 nm. The 100-nm-thick SRO layer was grown at 600 °C and 0.13 mbar O_2 at a target-to substrate distance of 55 mm. The spot size of the laser was 3 mm^2, the laser energy density was 2.5 J cm^{-2} and the pulse repetition rate was 8 Hz. The parameters for the growth of the 100-nm-thick STO layer were taken from the literature [44].

2.2. Structural characterization

An X-ray diffractometer (Empyrean, Malvern PANalytical) with Cu$K\alpha_1$ radiation (λ = 1.5406 Å) was used to collect the θ-2θ patterns, rocking curves (RCs) and reciprocal-space maps (RSMs). A double-bounce Ge (2 2 0) hybrid monochromator was used on the incident-beam side. The PIXcel3D detector in 1D mode was used to capture and analyze the diffracted beam in θ-2θ scans and RSMs. The results of the RSMs are presented with contour plots of intensity versus Q in the reciprocal lattice unit (*r.l.u.*), where $Q = \lambda/2d$. RCs were collected with the detector in 0D mode and 111/256 channels open, in order to avoid overlapping with STO, while still collecting the full width of the PMN-PT.

The surface structure of the templates and the films was examined by an *in-situ* reflection high-energy electron diffraction (RHEED) system (STAIB Instruments) with an accelerating voltage of 30 kV. The patterns were analyzed using kSA 400 software (k-Space Associates). Atomic force microscopy (AFM, Veeco Dimension 3100 SPM) and scanning electron microscopy (SEM, field-emission gun microscope JEOL JSM-7600F) were employed to examine the morphology of the samples. The AFM images were processed using WSxM 4.0 software [21], which was also used to calculate the ironed surface area of the different templates. SEM was also used to extract the layer thicknesses from sample cross-sections.

The chemical composition (i.e. the stoichiometry) of the PMN-PT thin films was examined using quantitative electron-probe microanalysis by wavelength-dispersive X-ray spectroscopy (WDXS) that was performed using the analytical system Oxford Instruments INCA WAVE

attached to the SEM. The exact, optimized WDXS procedure for the measurements and analyses is described elsewhere [14,45].

2.3. Electrical characterization

The samples were measured in parallel plate capacitor geometry, where LNO or Nb-doped STO were used as bottom electrodes, while the top electrodes consisted of Au, sputtered using shadow masks with holes 475 μm and 600 μm in diameter. Electrodes with 475 μm diameter were used for dielectric and ferroelectric measurements, while electrodes with 600 μm diameter were used to determine the piezoelectric properties of the films. Dielectric measurements were conducted at a frequency of 1 kHz and an AC amplitude of 100 mV using an LCR meter (Agilent 4284) with Cascade DCP-HTR probes. The ferroelectric properties were determined using a ferroelectric test system (Radiant Precision LC materials analyzer), operating in virtual ground mode. A series of double triangular bipolar waveforms was applied at a frequency of 10 Hz and an amplitude between 1 V and 10 V.

The piezoelectric characteristics of the capacitors were determined using a double-beam laser interferometer (aixDBLI, aixACCT). The longitudinal effective piezoelectric coefficient ($d_{33,f}$) was measured at different DC fields by superimposing a small AC signal with amplitude of 0.5 V and frequency of 1 kHz on a stepwise DC signal with maximal amplitude corresponding to ± 150 kV cm^{-1}. The electrode size was selected in accordance to the substrate thickness and its Poisson's ratio to avoid the additional contribution to the measured strain due to the substrate deformation.

3. Results and discussion

3.1. Stabilization of the perovskite phase on LNO/STO templates

As we have shown in our previous work [14], thin films grown directly on TiO_2-terminated STO substrates from a stoichiometric PMN-33PT target contain a large amount of pyrochlore impurities, while single-phase films can be grown using a target with 20 mol. % PbO excess. The results of this study show that by adding an intermediate LNO electrode layer it is possible to grow phase-pure PMN-33PT thin films even by using a stoichiometric target. A comparison of XRD patterns of PMN-33PT thin films grown directly on STO (samples *S0Pb* and *S20Pb*) and via LNO (samples *L0Pb* and *L20Pb*) is shown in Fig. 1. Samples *S20Pb* and *L20Pb* were grown using a target with 20 mol. % PbO excess, while samples *S0Pb* and *L0Pb* were prepared from the stoichiometric target, i.e. target with 0 mol. % PbO excess. The ratio of the integrals for (4 0 0) pyrochlore and (0 0 2) PMN-33PT was

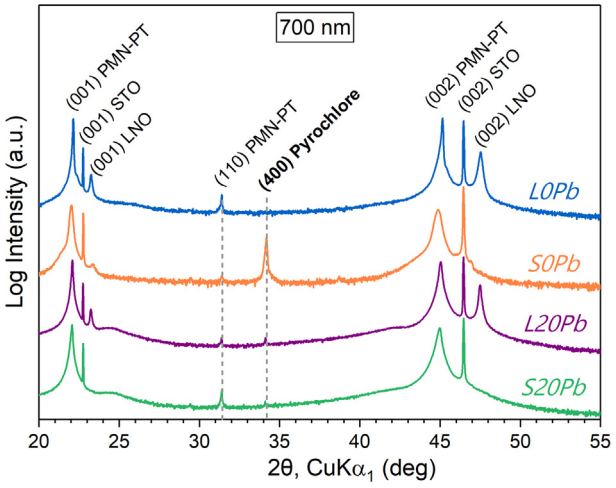

Fig. 1. XRD patterns of PMN-33PT samples prepared directly on STO and on LNO/STO.

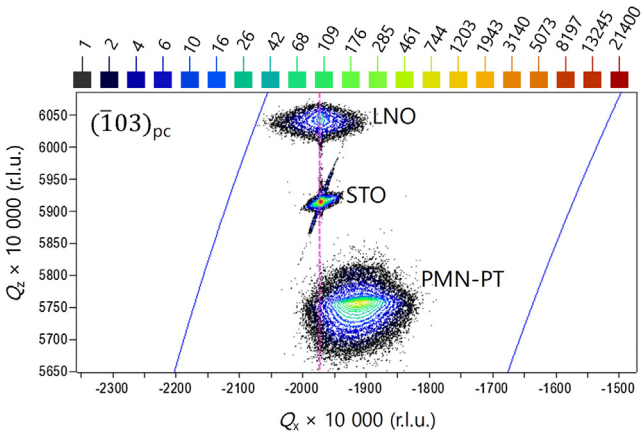

Fig. 2. RSM around the $(\bar{1}\ 0\ 3)_{pc}$ reflections in sample L0Pb. The pink dashed line indicates that the LNO electrode is fully strained to the STO substrate, whereas the PMN-PT layer is relaxed. (For interpretation of the references to colour in this figure legend, the reader is referred to the web version of this article.)

2×10^{-2} in sample *S0Pb*, whereas the signal for (4 0 0) Py in sample *L0Pb* was on the level of the noise, i.e. no pyrochlore phase was detected. The phase composition of samples *S20Pb* and *L20Pb* is highly comparable, but it should be noted that the process window for the preparation of high-quality PMN-33PT expands vastly upon the use of LNO as the bottom electrode. Specifically, in addition to higher flexibility regarding the PbO excess in the target, the temperature window for depositing phase-pure PMN-33PT broadened by at least 20 °C.

In order to find the mechanism behind this phase stabilization, we performed a series of analyses and further experiments where we tried to separate the individual factors. Starting with the influence of the difference in the unit cell parameters of bulk LNO (a_{pc} = 3.84 Å) and STO (a = 3.91 Å), which would lead to different mismatches with PMN-33PT, we analyzed the thin-film lattice parameters of the LNO electrodes by RSM. As it is shown in the RSM in Fig. 2, the peak positions of STO and LNO are found at the same Q_x value, which means that the LNO layer is fully strained to the STO, i.e. that their in-plane lattice parameters match. This result implies that the difference in the in-plane lattice mismatches is not involved in the stabilization mechanism. In principle, the difference in the out-of-plane lattice parameters of the STO and LNO could also influence the growth of PMN-PT, as the surfaces of the templates are not ideally flat. Due to the presence of steps and other surface features, a superior out-of-plane lattice match could facilitate phase-pure PMN-PT growth. The measured out-of-plane lattice parameter of the LNO layer was 3.83 Å. As this value leads to a larger PMN-PT/LNO mismatch, as compared to PMN-PT/STO, the different out-of-plane parameter of the LNO template could not account for the stabilization of the perovskite phase. Furthermore, since the LNO layer is strained, the difference between the thermal expansion coefficients of LNO and STO does not play a role in the phase stabilization of PMN-PT either.

Having excluded the difference in the lattice parameters as the main reason for the change in the stability of the perovskite phase, we considered other possibilities. In order to find out, whether the change of the interface chemistry is responsible for the enhanced sticking of Pb-based species and thus a suppression of the pyrochlore phase formation, we used a different bottom electrode, namely SRO. The assumption that a change in the surface chemistry would lead to a change in the growth of the PMN-PT was based on the observations made on the growth of BFO [46] and SRO [47], which also contain volatile constituents. In these systems, it has been reported that the change in STO termination leads to a change in the growth mode, due to a change in the surface diffusivity. A large influence of the different terminations on the nucleation and growth processes has been observed in other systems, such

as $YBa_2Cu_3O_{7-\delta}$ (YBCO) [48] as well. The aforementioned studies on BFO, SRO and YBCO were focused on the growth modes, rather than the phase composition of the films. Furthermore, they mostly involved the growth of ultra-thin films.

Owing to the high volatility of RuO_x species, PLD-derived epitaxial SRO has been shown to be SrO-terminated at deposition conditions, similar to the ones used in this study [31,32,47]. Therefore, SRO/STO templates, such as the ones used in this study, provide an interface similar to that of SrO-terminated STO. Because of its close lattice-matching with STO, SRO is often used as a bottom electrode for the preparation of high-quality perovskite thin films. Based on literature reports SRO/STO templates have been used to prepare pyrochlore-free PMN-33PT thin films with PLD from stoichiometric targets [13,41,42]. It is important to note that the thickness of the PMN-33PT films in these reports was 300 nm. When we prepared 300-nm-thick PMN-33PT on SRO/STO using the stoichiometric target, the films also appeared to be pyrochlore-free, according to XRD analysis (**Fig. S1**), which was an improvement with respect to the 300 nm PMN-33PT/STO, where a small amount of pyrochlore was identified. However, when we prepared thicker films, comparable to the ones shown in Fig. 1, a large amount of pyrochlore was formed in PMN-33PT on SRO/STO, when using the target without PbO excess (sample *SROO0Pb*). No pyrochlore was detected when we used the target with 20 mol. % PbO excess (Fig. S1). The large difference between the thinner and the thicker films is related to inverted conical shape of the pyrochlore inclusions. As the film growth progresses their volume largely increases. Therefore, thinner films contain a smaller volume of pyrochlore, which could be below the detection limit of laboratory diffractometers. At higher thicknesses, using the same deposition parameters, the amount of pyrochlore exceeds the detection limit. Additionally, by increasing the thickness of the films they are exposed to elevated temperatures for a larger amount of time, which could lead to changes in the structure of the films, due to the presence of volatile PbO_x and RuO_x species. Note that, like LNO, the SRO was also fully strained to the STO substrate, as shown by the RSM in **Fig. S2**.

To summarize, the use of an intermediate SRO layer did not significantly enhance the stability of the perovskite phase, as compared to growth on bare STO. For thicknesses above 500 nm, PbO excess was required to prepare phase-pure PMN/PT films on both STO and SRO/STO, whereas the LNO/STO template enabled phase-pure growth from the stoichiometric target.

In order to find the differences between the STO, LNO/STO and SRO/STO templates, we examined their surfaces by AFM. Representative images together with the corresponding RHEED patterns are shown in Fig. 3. The STO (panel a)) exhibited smooth steps with unit-cell-size step height. The latter was also the case in SRO/STO (panel b)), which exhibited wider steps. Despite the presence of small holes the SRO/STO template had a relatively low root-mean-square roughness (RMS). The surface of the 100-nm-thick LNO layer (panel c)), on the other hand, consisted of small granular structures. The STO steps were no longer visible, as the growth of LNO transformed from 2D to 3D after a few nanometers. This 3D nature of the surface was already indicated by the transmission pattern that was obtained using *in-situ* RHEED after the deposition of the LNO layer, as shown in the inset. The roughness is therefore significantly larger as compared to the STO and SRO/STO templates. Based on these results, the difference in morphology has the most pronounced effect on the phase composition of the PMN-PT thin films. As thick LNO has a rougher surface it enhances the sticking probability of Pb-based species and consequently stabilizes the perovskite structure through a mechanism similar to that observed in the growth of PMN-PT on miscut substrates [7,19,20], whereby in our case the stabilization was even stronger on LNO. The XRD patterns of PMN-33PT thin films grown on vicinal substrates (**Fig. S3**) revealed only a slight improvement of the stability of the perovskite phase, decreasing the amount of PbO excess required for phase-pure growth by 5 mol. %.

In order to verify this mechanism, we first prepared an LNO/STO template with a relatively smooth surface. Owing to the aforementioned 3D growth mode that sets in at an early stage in the growth, we deposited an ultrathin (~1.5 nm) layer of LNO. The number of pulses required to obtain the ultrathin film was derived from the number of pulses required to grow the 100-nm-thick film, as determined by cross-sectional view SEM analysis. The surface of this template was relatively flat, attested by the relatively low RMS value and streaky RHEED pattern shown in Fig. 4**(a)**. Furthermore, the outlines of the underlying STO steps are still visible in the AFM image. We used this template to grow a PMN-33PT thin film, using the stoichiometric target. This sample was named *LUT0Pb*. The resulting XRD pattern (**Fig. S4**) shows that there was no improvement in the phase composition of the film, as compared to sample *S0Pb*. Therefore, comparable morphology of the STO and LNO/STO templates yielded comparable results. For additional confirmation of this interface-roughness-driven stabilization mechanism, we prepared an STO buffer layer. This way the material would match the STO substrate, however, we could vary the surface morphology. In this way a morphology similar to that of 100-nm-thick LNO was obtained. We used the parameters from Díaz-Fernandez et al. [44] to deposit STO with a comparable roughness (RMS ≈ 1 nm). The AFM image and RHEED pattern of the STO/Nb:STO template are shown in Fig. 4 **b)**. The substrate and layer peak positions in the XRD pattern matched, indicating that there was no off-stoichiometry in the STO layer. The results shown in **Fig. S5** confirm that the roughening of the surface brings about a significant change in the phase composition of

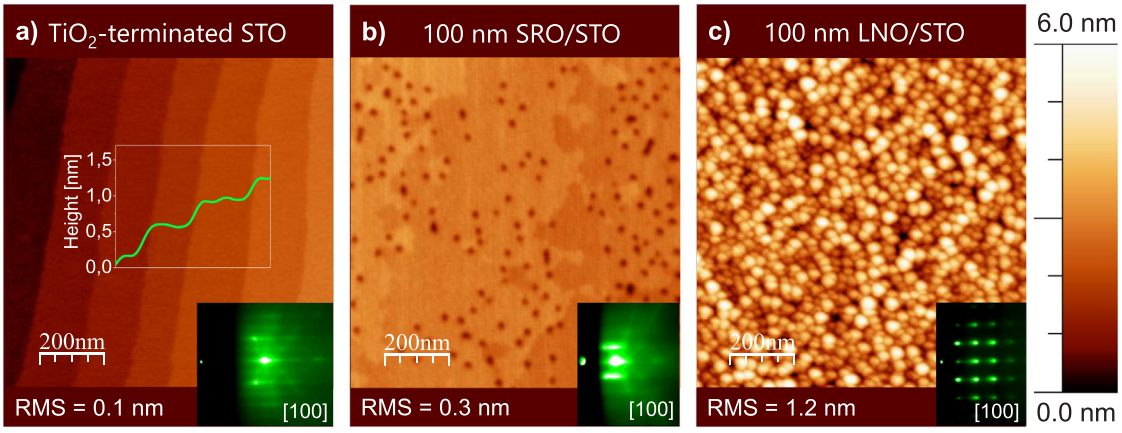

Fig. 3. AFM images and RHEED patterns of different templates for the PMN-PT thin films: (a) a treated STO substrate (the inset shows a line profile across the steps), (b) SRO/STO and c) LNO/STO.

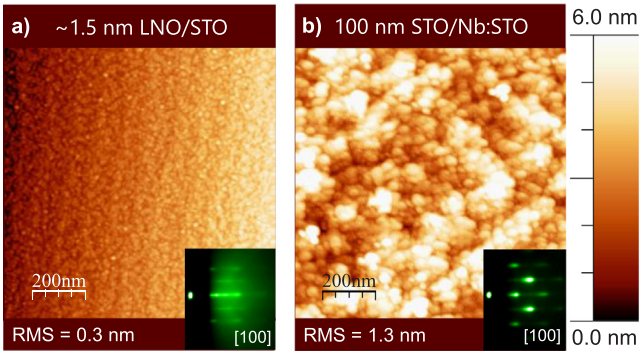

Fig. 4. AFM images and RHEED patterns of (a) ultra-thin LNO/STO and (b) STO/Nb:STO templates.

the PMN-PT. A comparison of the two samples prepared from the stoichiometric PMN-33PT target: (i) sample *S0Pb*, prepared directly on STO and (ii) sample *SH0Pb*, prepared on an STO buffer layer, reveals that inserting the homoepitaxial STO layer resulted in lowering the concentration of pyrochlore by a factor of 40.

A comparison of the ironed surface area of all of the templates and the ratio between the integrated area of the (4 0 0) reflection of the pyrochlore phase and the (0 0 2) reflection of the perovskite phase in the corresponding thin films, is shown in Fig. 5. All of the films were prepared using the PMN-33PT target without PbO excess. Samples *SRO0Pb* and *4deg0Pb* were prepared on SRO/STO and vicinal STO, respectively. As the ironed surface area increases, the pyrochlore/perovskite ratio decreases monotonously. A template with a larger surface area provides more binding sites for the arriving species, increasing the activation energy for desorption, which keeps a sufficient amount of Pb-based species in the film.

3.2. Chemical composition of the films

We examined the chemical composition of the four samples with the smallest amount of secondary phase by WDXS (Fig. 6). These were samples *S20Pb* and *L20Pb*, prepared using the PMN-33PT target with 20 mol. % PbO excess and samples *L0Pb* and *SH0Pb*, prepared using the stoichiometric PMN-33PT target. Despite the phase composition of samples being comparable according to the XRD patterns, minor quantities of secondary phases could remain undetected by XRD. Furthermore, compositional differences between the PMN-PT layers themselves can also exist, as a small amount of off-stoichiometry can be accommodated by the perovskite structure.

The results of the WDXS analysis (Fig. 6) showed that films prepared from the Pb-rich targets both exhibited a surplus of Pb. Of the 20 mol. % excess added, approximately 5 mol. % of excess Pb remained in the film. Taking into account experimental uncertainty i.e. the error bars, the concentration of Pb in *L0Pb* is completely stoichiometric. Sample *SH0Pb* is slightly Pb-deficient, which was expected, given that it was the only one of the four samples, whose pyrochlore concentration was above the limit of detection in XRD analysis. All of the films exhibit a deficiency in Mg concentration. This deficiency is more pronounced in films prepared from the target with PbO excess, which confirms the compensation mechanism observed in our previous work [14]. Most of the films were slightly Ti-deficient and Nb-rich. The calculated oxygen concentrations were 59.8–60.2 at.%, which is highly consistent to regular perovskite stoichiometry of 60 at.%.

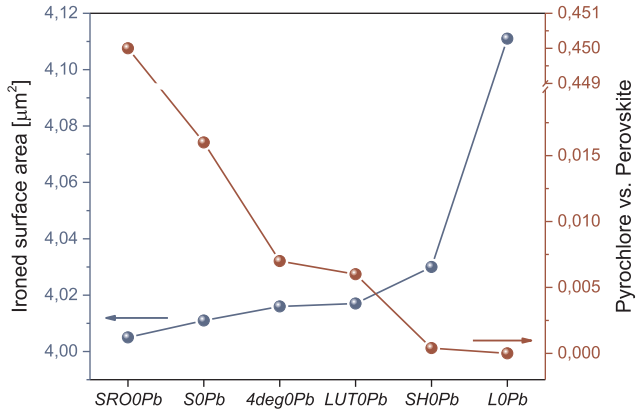

Fig. 5. Ironed surface area of the template and ratio between the (4 0 0) pyrochlore and (0 0 2) PMN-33PT peaks from the θ-2θ scans.

3.3. Piezoelectric, dielectric and ferroelectric properties

We also compared the electrical properties of the four samples from the previous subsection. The dielectric and ferroelectric properties are shown in Fig. 7. All samples exhibited dielectric losses between 0.04 and 0.07. Frequency dependence measurements of the relative permittivity and dielectric losses for all four samples are shown in **Fig. S6**. Sample *L0Pb* exhibited the highest relative permittivity (ε_r = 2350), however, the dielectric breakdown strength (10 kV cm^{-1}) of this film was too low to obtain saturated *P–E* loops, as shown in the inset of the graph in panel (b) of Fig. 7. This was also the case in sample *SH0Pb*. The dielectric breakdown strength of sample *S20Pb* was ~100 kV cm^{-1}. Sample *L20Pb* exhibited the highest dielectric breakdown strength (1000 kV cm^{-1}), thereby yielding a maximum polarization value of P_{max} = 50 µC cm^{-2} (not shown). All of the *P–E* loops were relatively slim, due to the presence of the relaxor-type PMN component.

The low dielectric breakdown strength of sample *SH0Pb* can be attributed to the presence of the pyrochlore inclusions, the concentration of which was the highest among the four tested samples. The origin of the low dielectric breakdown strength of sample *L0Pb* is less clear, as XRD and WDXS analysis pointed to a near-perfect perovskite structure. Compared to samples *S20Pb* and *L20Pb*, the stoichiometry of sample *L0Pb* is closer to the nominal one. This could account for the enhanced relative permittivity value of this sample. Despite the apparently superior intrinsic properties of sample *L0Pb*, it is possible that a poorer microstructure, larger defect concentrations or inhomogeneities lead to poorer dielectric breakdown strength. Conductive paths could be created under the relatively high electrical fields required to obtain (saturated) hysteresis loops. Another possible explanation is related to the types of extended defects formed in perovskites such as PMN-PT. As we have previously shown [14], PMN-PT films grown using PbO-rich targets, form extended PbO-rich defects, such as out-of-phase boundaries. It is possible that these types of defects are also formed under certain deposition conditions in films which contain an overall stoichiometric amount of Pb. This would result in a Pb-poor matrix. The correlation between the stoichiometry, microstructure and the electrical properties of PMN-PT thin films will be addressed in our future research.

We also measured the $d_{33,f}$ of samples *S20Pb* and *L20Pb* (Fig. 8). The internal bias field in these samples, indicated by the lateral shifts of the *P–E* and $d_{33,f}$–*E* hysteresis loops, could be related to the defects introduced into the layers by the sputtering of the top electrodes [49]. On the other hand, as the shift was not observed in samples *S0Pb* and *L0Pb*, it could also be related to the excess Pb or other defects present in the samples prepared from the Pb-rich targets. The maximum $d_{33,f}$ value of *L20Pb* was 90 pm V^{-1}. The highest $d_{33,f}$ value in *S20Pb* was 60 pm V^{-1}. Therefore, *L20Pb* exhibited the best properties in all regards, leading to the conclusion that the rough PMN-PT/LNO interface does not have a negative effect on the functional properties. This corroborates the results of the chemical and structural analysis. The latter revealed that the mosaicity of *S20Pb* and *L20Pb* was comparable, the full widths at half maximums of the rocking curve measurements were 0.49° and 0.42°, respectively.

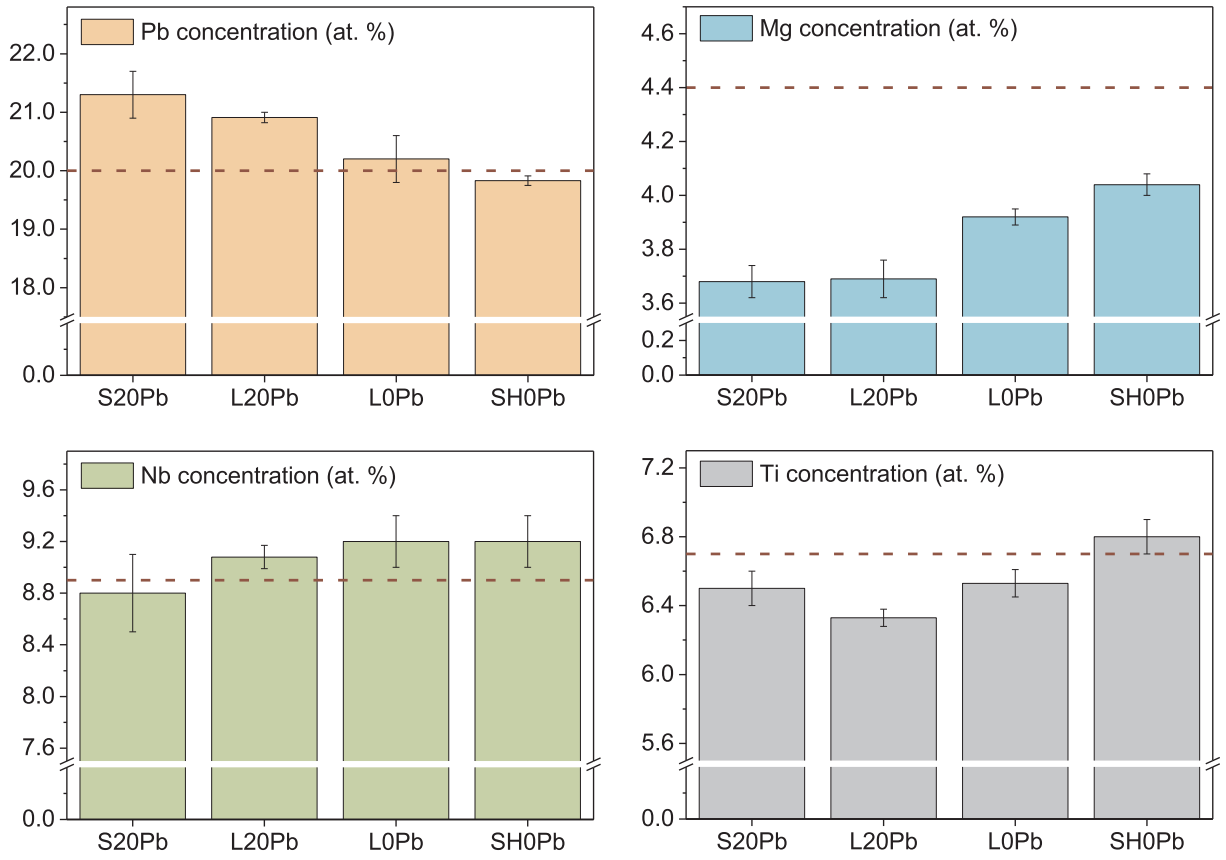

Fig. 6. Concentrations of individual elements as determined by WDXS analysis of selected samples. The dashed line represents the standard PMN-33PT stoichiometric values.

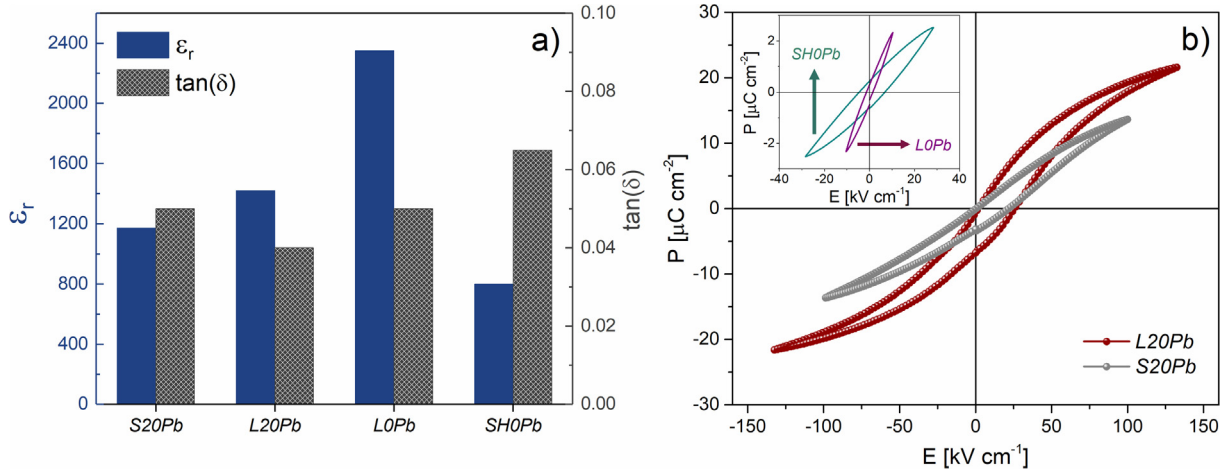

Fig. 7. (a) Relative permittivity and losses, and (b) P–E loops of the selected four samples.

4. Conclusions

We found that LNO strongly stabilizes the perovskite phase, expanding the process window for obtaining pyrochlore-free PMN-PT thin films. Using LNO, we were able to prepare single-phase films with thicknesses ~1 μm even from targets without PbO excess. Our results indicate that the main mechanism responsible for the enhanced stability is related to the relatively rough surface of the LNO/STO template, which offers more binding sites for Pb-based species. It is important to note that the higher interface roughness of PMN-PT/LNO (as compared to the PMN-PT/STO interface) does not lead to a higher defect density in the PMN-PT film. In fact, the film grown on LNO/STO exhibits a slightly lower mosaicity. Furthermore, the electrical properties are also improved, when PMN-PT is grown on LNO/STO. By understanding the mechanism, we were also able to significantly suppress the formation of the pyrochlore phase in the PMN-PT film prepared on STO by first depositing a homoepitaxial layer with a high surface roughness.

These results demonstrate a means of maintaining a larger quantity of volatile elements the thin films, which has important implications for the growth of high-quality Pb-based films, as well as in other Pb-free systems such as $Na_{0.5}Bi_{0.5}TiO_3$ or $AgNb_{1-x}Ta_xO_3$.

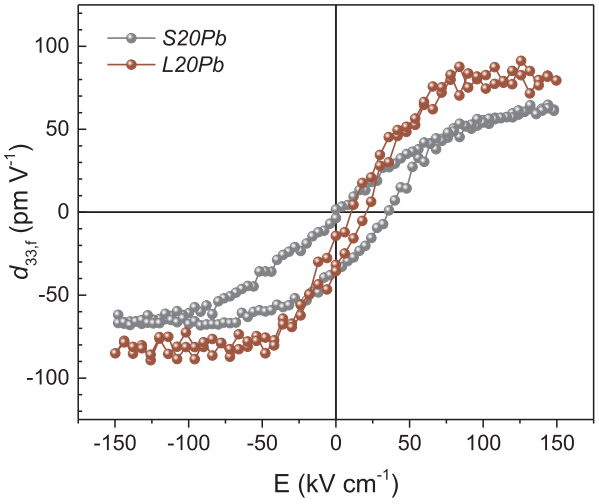

Fig. 8. Longitudinal piezoelectric response of samples S20Pb and L20Pb.

CRediT authorship contribution statement

Urška Gabor: Conceptualization, Investigation, Writing - original draft, Writing - review & editing, Visualization, Project administration. **Damjan Vengust:** Investigation, Resources. **Zoran Samardžija:** Methodology, Formal analysis, Investigation. **Aleksander Matavž:** Investigation. **Vid Bobnar:** Supervision, Funding acquisition. **Danilo Suvorov:** Supervision, Funding acquisition. **Matjaž Spreitzer:** Conceptualization, Writing - review & editing, Supervision, Project administration, Funding acquisition.

Declaration of Competing Interest

The authors declare that they have no known competing financial interests or personal relationships that could have appeared to influence the work reported in this paper.

Acknowledgements

David Fabijan is gratefully acknowledged for his assistance with dielectric and ferroelectric measurements. This research is financed by the Slovenian Research Agency, Slovenia [grant numbers PR-06231, J2-9237, J2-1740]; and M-Era.Net, European Union [grant number 3330-17-500100 (project SIOX)].

Appendix A. Supplementary material

See Appendix A: Supplementary material for θ-2θ patterns of PMN-33PT thin films grown on SRO/STO, vicinal STO, ultra-thin LNO/STO and homoepitaxial STO /Nb:STO, as well as RSM of PMN-33PT/SRO/STO. Supplementary data to this article can be found online at https://doi.org/10.1016/j.apsusc.2020.145787.

References

[1] S. Park, T.R. Shrout, Ultrahigh strain and piezoelectric behavior in relaxor based ferroelectric single crystals, J. Appl. Phys. 82 (1997) 1804–1811, https://doi.org/10.1063/1.365983.
[2] H. Fu, R.E. Cohen, Polarization rotation mechanism for ultrahigh electrochemical response in single-crystal piezoelectrocs, Lett. to Nat. 403 (2000) 281–283. www.nature.com (accessed August 20, 2018).
[3] Z. Kutnjak, J. Petzelt, R. Blinc, The giant electromechanical response in ferroelectric relaxors as a critical phenomenon, Nature 441 (2006) 956–959, https://doi.org/10.1038/nature04854.
[4] Y. Zhang, D. Xue, H. Wu, X. Ding, T. Lookman, X. Ren, Adaptive ferroelectric state at morphotropic phase boundary: Coexisting tetragonal and rhombohedral phases, Acta Mater. 71 (2014) 176–184, https://doi.org/10.1016/j.actamat.2014.03.007.
[5] H. Liu, J. Chen, L. Fan, Y. Ren, Z. Pan, K.V. Lalitha, J. Rödel, X. Xing, Critical role of monoclinic polarization rotation in high-performance perovskite piezoelectric materials, Phys. Rev. Lett. 119 (2017) 017601, , https://doi.org/10.1103/PhysRevLett. 119.017601.
[6] F. Li, S. Zhang, T. Yang, Z. Xu, N. Zhang, G. Liu, J. Wang, J. Wang, Z. Cheng, Z.-G. Ye, J. Luo, T.R. Shrout, L.-Q. Chen, The origin of ultrahigh piezoelectricity in relaxor-ferroelectric solid solution crystals, Nat. Commun. 7 (2016) 13807, https://doi.org/10.1038/ncomms13807.
[7] S.H. Baek, J. Park, D.M. Kim, V.A. Aksyuk, R.R. Das, S.D. Bu, D.A. Felker, J. Lettieri, V. Vaithyanathan, S. Bharadwaja, N. Bassiri-Gharb, Y.B. Chen, H.P. Sun, C.M. Folkman, H.W. Jang, D.J. Kreft, S.K. Streiffer, R. Ramesh, X.Q. Pan, S. Trolier-McKinstry, D.G. Schlom, M.S. Rzchowski, R. Blick, C.B. Eom, Giant piezoelectricity on Si for hyperactive MEMS, Science 334 (2011) 958–961, https://doi.org/10.1126/science.1207186.
[8] S. Pandya, J. Wilbur, J. Kim, R. Gao, A. Dasgupta, C. Dames, L.W. Martin, Pyroelectric energy conversion with large energy and power density in relaxor ferroelectric thin films, Nat. Mater. 17 (2018) 432–438, https://doi.org/10.1038/s41563-018-0059-8.
[9] A.S. Mischenko, Q. Zhang, R.W. Whatmore, J.F. Scott, N.D. Mathur, Giant electrocaloric effect in the thin film relaxor ferroelectric 0.9 $PbMg_{1/3}Nb_{2/3}O_3$-0.1 $PbTiO_3$ near room temperature, Appl. Phys. Lett. 89 (2006) 1–4, https://doi.org/10.1063/1.2405889.
[10] M. Mietschke, P. Chekhonin, C. Molin, S. Gebhardt, S. Fähler, K. Nielsch, L. Schultz, R. Hühne, Influence of the polarization anisotropy on the electrocaloric effect in epitaxial PMN-PT thin films, J. Appl. Phys. 120 (2016) 114102, , https://doi.org/10.1063/1.4962858.
[11] X. Wang, L. Zhang, X. Hao, S. An, High energy-storage performance of 0.9$PbMg_{1/3}Nb_{2/3}O_3$-0.1$PbTiO_3$ relaxor ferroelectric thin films prepared by RF magnetron sputtering, Mater. Res. Bull. 65 (2015) 73–79, https://doi.org/10.1016/j.materresbull.2015.01.038.
[12] J. Wang, K.H. Wong, H.L.W. Chan, C.L. Choy, Composition control and electrical properties of PMN-PT thin films around the morphotropic boundary, Appl. Phys. A Mater. Sci. Process. 79 (2004) 551–556, https://doi.org/10.1007/s00339-003-2355-6.
[13] M. Boota, E.P. Houwman, M.D. Nguyen, G. Lanzara, G. Rijnders, Effect of fabrication conditions on phase formation and properties of epitaxial ($PbMg_{1/3}Nb_{2/3}O_3$) 0.67-$PbTiO_3$ thin films on $SrTiO_3$, AIP Adv. 6 (2016) 055303, https://doi.org/10.1063/1.4948793.
[14] U. Gabor, M. Spreitzer, H. Uršič, E. Tchernychova, Z. Samardžija, W.J. Wu, D. Suvorov, Structural peculiarities of 0.67 $Pb(Mg_{1/3}Nb_{2/3})O_3$–0.33 $PbTiO_3$ thin films grown directly on $SrTiO_3$ substrates, J. Eur. Ceram. Soc. 38 (2018) 4453–4462, https://doi.org/10.1016/j.jeurceramsoc.2018.06.013.
[15] C. Tantigate, A. Safari, Preparation of $Pb(Mg_{1/3}Nb_{2/3})O_3$-$PbTiO_3$ thin films on silicon substrates by pulsed laser deposition, Microelectron. Eng. 29 (1995) 115–118, https://doi.org/10.1016/0167-9317(95)00127-1.
[16] J.-P. Maria, W. Hackenberger, S. Trolier-McKinstry, Phase development and electrical property analysis of pulsed laser deposited $Pb(Mg_{1/3}Nb_{2/3})O_3$–$PbTiO_3$ (70/30) epitaxial thin films, J. Appl. Phys. 84 (1998) 5147–5154, https://doi.org/10.1063/1.368809.
[17] S.S. Kumar, R. Reshmi, N.V. Joshy, A.C. Saritha, M.K. Jayaraj, Optical Emission Spectroscopic Analysis of Plasma Plume during Pulsed Laser Deposition of PZT, J. At. Mol. Phys. 2014 (2014) 125843, , https://doi.org/10.1155/2014/125843.
[18] J. Levoska, M. Tyunina, A. Sternber, S. Leppavouri, Structural characterization ofrelaxor ferroelectric $PbMg_{1/3}Nb_{2/3}O_3$-$PbTiO_3$ thin film heterostructures deposited by pulsed laser ablation, Appl. Phys. A 70 (2000) 269–274, https://doi.org/10.1080/10584589808202090.
[19] S.D. Bu, M.K. Lee, C.B. Eom, W. Tian, X.Q. Pan, S.K. Streiffet, J.J. Krajewski, Perovskite phase stabilization in epitaxial $Pb(Mg_{1/3}Nb_{2/3})O_3$-$PbTiO_3$ films by deposition onto vicinal (001) $SrTiO_3$ substrates, Appl. Phys. Lett. 79 (2001) 3482–3484, https://doi.org/10.1063/1.1414293.
[20] P. Chekhonin, M. Mietschke, D. Pohl, F. Schmidt, S. Fähler, W. Skrotzki, K. Nielsch, R. Hühne, Effect of substrate miscut on the microstructure in epitaxial $Pb(Mg_{1/3}Nb_{2/3})O_3$-$PbTiO_3$ thin films, Mater. Charact. 129 (2017) 234–241, https://doi.org/10.1016/j.matchar.2017.05.003.
[21] Z.-J. Wang, K. Kikuchi, R. Maeda, Effect of Pb Content in Target on Electrical Properties of Laser Ablation Derived Lead Zirconate Titanate Thin Films, Jpn. J. Appl. Phys. 39 (2000) 5413–5417, https://doi.org/10.1143/JJAP.39.5413.
[22] D. Mukherjee, R. Hyde, P. Mukherjee, H. Srikanth, S. Witanachchi, Role of dual-laser ablation in controlling the Pb depletion in epitaxial growth of Pb(Zr0.52Ti0.48)O3 thin films with enhanced surface quality and ferroelectric properties, J. Appl. Phys. 111 (2012) 064102. https://doi.org/10.1063/1.3694035.
[23] D. Mukherjee, R. Hyde, M. Hordagoda, N. Bingham, H. Srikanth, S. Witanachchi, P. Mukherjee, Challenges in the stoichiometric growth of polycrystalline and epitaxial PbZr0.52Ti0.48O3/La0.7Sr0.3MnO3 multiferroic heterostructures using pulsed laser deposition, J. Appl. Phys. 112 (2012) 064101. https://doi.org/10.1063/1.4751027.
[24] C.P. de Araujo, J.F. Scott, G.W. Taylor, Ferroelectric Thin Films: Synthesis and Basic Properties, in: Ferroelectr. Relat. Phenom., Gordon and Breach, 1996: pp. 193–230. https://doi.org/10.1080/10584589608012321.
[25] T. Nakamura, Y. Nakao, A. Kamisawa, H. Takasu, Preparation of $Pb(Zr, Ti)_O3$ thin films on electrodes including Ir_O2, Appl. Phys. Lett. 65 (1994) 1522–1524, https://doi.org/10.1063/1.112031.
[26] H.N. Al-Shareef, O. Auciello, A.I. Kingon, Electrical properties of ferroelectric thin-film capacitors with hybrid (Pt, Ru_O2) electrodes for nonvolatile memory applications, J. Appl. Phys. 77 (1995) 2146–2154, https://doi.org/10.1063/1.359572.
[27] A.K. Tagantsev, I. Stolichnov, E.L. Colla, N. Setter, Polarization fatigue in ferroelectric films: Basic experimental findings, phenomenological scenarios, and

microscopic features, J. Appl. Phys. 90 (2001) 1387, https://doi.org/10.1063/1.1381542.
[28] I. Stolichnov, A. Tagantsev, N. Setter, J.S. Cross, M. Tsukada, Top-interface-controlled switching and fatigue endurance of (Pb, La)(Zr, Ti_iO3 ferroelectric capacitors, Appl. Phys. Lett. 74 (1999) 3552–3554, https://doi.org/10.1063/1.124158.
[29] M.D. Nguyen, E.P. Houwman, M. Dekkers, G. Rijnders, Strongly Enhanced Piezoelectric Response in Lead Zirconate Titanate Films with Vertically-Aligned Columnar Grains, ACS Appl. Mater. Interfaces. 9849–9861 (2017), https://doi.org/10.1021/acsami.6b16470.
[30] Y.W. Li, Z.G. Hu, F.Y. Yue, G.Y. Yang, W.Z. Shi, X.J. Meng, J.L. Sun, J.H. Chu, Properties of highly (100) oriented Pb ($Mg_{1/3}Nb_{2/3}$)O_3-$PbTiO_3$ films on $LaNiO_3$ bottom electrodes, Appl. Phys. Lett. 91 (2007) 89–92, https://doi.org/10.1063/1.2822421.
[31] F. Johann, A. Morelli, D. Biggemann, M. Arredondo, I. Vrejoiu, Epitaxial strain and electric boundary condition effects on the structural and ferroelectric properties of $BiFeO_3$ films, Phys. Rev. B. 8415 (2011) 094105, , https://doi.org/10.1103/PhysRevB.84.094105.
[32] Y.H. Chu, Q. He, C.H. Yang, P. Yu, L.W. Martin, P. Shafer, R. Ramesh, Nanoscale control of domain architectures in $BiFeO_3$ thin films, Nano Lett. 9 (2009) 1726–1730, https://doi.org/10.1021/nl900723j.
[33] S.P. Alpay, V. Nagarajan, L.A. Bendersky, M.D. Vaudin, S. Aggarwal, R. Ramesh, A.L. Roytburd, Effect of the electrode layer on the polydomain structure of epitaxial $PbZr_{0.2}Ti_{0.8}O_3$ thin films, J. Appl. Phys. 85 (1999) 3271, https://doi.org/10.1063/1.369670.
[34] V. Shelke, D. Mazumdar, G. Srinivasan, A. Gupta, The role of $SrRuO_3$ bottom layer in strain relaxation of $BiFeO_3$ thin films deposited on lattice mismatched substrates, J. Appl. Phys. 109 (2011) 07D914, https://doi.org/10.1063/1.3564940.
[35] J. Peräntie, M.S. Stratulat, J. Hannu, H. Jantunen, M. Tyunina, Enhancing polarization by electrode-controlled strain relaxation in $PbTiO_3$ heterostructures, APL Mater. 4 (2016) 016104, , https://doi.org/10.1063/1.4939790.
[36] C. Guerrero, F. Sánchez, C. Ferrater, J. Roldán, M.V. García-Cuenca, M. Varela, Pulsed laser deposition of epitaxial $PbZr_xTi_{1-x}O_3$ ferroelectric capacitors with $LaNiO_3$ and $SrRuO_3$ electrodes, Appl. Surf. Sci. 168 (2000) 219–222, https://doi.org/10.1016/S0169-4332(00)00601-2.
[37] D.H.A. Blank, M. Dekkers, G. Rijnders, Pulsed laser deposition in Twente: from research tool towards industrial deposition, J. Phys. D. Appl. Phys. 47 (2014) 034006, https://doi.org/10.1088/0022-3727/47/3/034006.
[38] M.D. Nguyen, R. Tiggelaar, T. Aukes, G. Rijnders, G. Roelof, Wafer-scale growth of highly textured piezoelectric thin films by pulsed laser deposition for micro-scale sensors and actuators, J. Phys. Conf. Ser. 922 (2017), https://doi.org/10.1088/1742-6596/922/1/012022.
[39] M. Dekkers, M. Nguyen, N. Hildenbrand, S. Abel, F. Eltes, J. Fompeyrine, P. Wittendorp, Wafer level integration of epitaxial piezoelectric thin films for novel NEMS, MEMS and MOEMS applications, Adv. Mater. - TechConnect Briefs 2017 (4) (2017) 55–58.
[40] S.-B. Kim, H. Park, S.-H. Kim, H.C. Wikle, J.-H. Park, D.-J. Kim, Comparison of MEMS PZT Cantilevers Based on d33 and d31 Modes for Vibration Energy Harvesting, J. Microelectromechanical Syst. 22 (2013) 26–33, https://doi.org/10.1109/JMEMS.2012.2213069.
[41] M. Boota, E.P. Houwman, M. Dekkers, M.D. Nguyen, K.H. Vergeer, G. Lanzara, G. Koster, G. Rijnders, Properties of epitaxial, (001)- and (110)-oriented ($PbMg_{1/3}Nb_{2/3}O_3$)$_{2/3}$-($PbTiO_3$)$_{1/3}$ films on silicon described by polarization rotation, Sci. Technol. Adv. Mater. 17 (2016) 45–57, https://doi.org/10.1080/14686996.2016.1140306.
[42] M. Boota, E.P. Houwman, M. Dekkers, M. Nguyen, G. Rijnders, Epitaxial $Pb(Mg_{1/3}Nb_{2/3})O_3$-$PbTiO_3$ (67/33) thin films with large tunable self-bias field controlled by a $PbZr_{1-x}Ti_xO_3$ interfacial layer, Appl. Phys. Lett. 104 (2014) 182909, , https://doi.org/10.1063/1.4874978.
[43] G. Koster, B.L. Kropman, G.J.H.M. Rijnders, D.H.A. Blank, H. Rogalla, Quasi-ideal strontium titanate crystal surfaces through formation of strontium hydroxide, Appl. Phys. Lett. 73 (1998) 2920–2922, https://doi.org/10.1063/1.122630.
[44] D. Diaz-Fernandez, M. Spreitzer, T. Parkelj, D. Suvorov, Multi-stage pulsed laser deposition of high quality epitaxial ultra-thin $SrTiO_3$ on Si substrates, Appl. Surf. Sci. 455 (2018) 227–235, https://doi.org/10.1016/j.apsusc.2018.05.173.
[45] Z. Samardžija, J.-H. Jeon, M. Čeh, Microstructural and compositional study of a bulk $Pb(Mg_{1/3}Nb_{2/3})O_3$–$PbTiO_3$ single crystal grown from a $BaTiO_3$ seed, Mater. Charact. 58 (2007) 534–543, https://doi.org/10.1016/j.matchar.2006.10.003.
[46] A. Solmaz, M. Huijben, G. Koster, R. Egoavil, N. Gauquelin, G. Van Tendeloo, J. Verbeeck, B. Noheda, G. Rijnders, Domain Selectivity in $BiFeO_3$ Thin Films by Modified Substrate Termination, Adv. Funct. Mater. 26 (2016) 2882–2889, https://doi.org/10.1002/adfm.201505065.
[47] G. Rijnders, D.H.A. Blank, J. Choi, C.B. Eom, Enhanced surface diffusion through termination conversion during epitaxial $SrRuO_3$ growth, Appl. Phys. Lett. 84 (2004) 505–507, https://doi.org/10.1063/1.1640472.
[48] J.M. Huijbregtse, J.H. Rector, B. Dam, Effect of the two (100) $SrTiO_3$ substrate terminations on the nucleation and growth of $YBa_2Cu_3O_{7-\delta}$ thin films, Phys. C Supercond. Appl. 351 (2001) 183–199, https://doi.org/10.1016/S0921-4534(00)01616-6.
[49] A. Matavz, J. Kovač, M. Cekada, B. Malič, V. Bobnar, Enhanced electrical response in ferroelectric thin film capacitors with inkjet-printed $LaNiO_3$ electrodes, Appl. Phys. Lett. 113 (2018) 12904, https://doi.org/10.1063/1.5037027.